2870 Vol. 42, No. 15 / August 1 2017 / Optics Letters Letter

Optics Letters

Generation of continuously rotating polarization by combining cross-polarizations and its application in surface structuring

Billy Lam,[1] Jihua Zhang,[1] and Chunlei Guo[1,2,*]

[1]The Institute of Optics, University of Rochester, Rochester, New York 14627, USA
[2]Changchun Institute of Optics, Fine Mechanics, and Physics, Changchun 130033, China
*Corresponding author: guo@optics.rochester.edu

Received 23 March 2017; accepted 25 June 2017; posted 29 June 2017 (Doc. ID 291227); published 17 July 2017

In this study, we develop a simple but highly effective technique that generates a continuously varying polarization within a laser beam. This is achieved by having orthogonal linear polarizations on each side of the beam. By simply focusing such a laser beam, we can attain a gradually and continuously changing polarization within the entire Rayleigh range due to diffraction. To demonstrate this polarization distribution, we apply this laser beam onto a metal surface and create a continuously rotating laser induced periodic surface structure pattern. This technique provides a very effective way to produce complex surface structures that may potentially find applications, such as polarization modulators and metasurfaces.

OCIS codes: (260.5430) Polarization; (320.7120) Ultrafast phenomena.

https://doi.org/10.1364/OL.42.002870

With the advancement in liquid-crystal spatial light modulators (SLM), generation of vectorial optical fields with complex spatial distributions of phase, amplitude, and polarization is now a possibility [1]. Recently, optical vector beams with various spatial distributions of polarization have been used to directly fabricate complex surface structures [2–7]. Some of the most commonly used optical vector beams are radially and azimuthally polarized beams [5–7]. For example, the use of two SLMs and wave plates for complete control of the beam wavefront and polarization for microprocessing has previously been demonstrated [8]. However, such a method requires all neighbor SLM pixels to take on different values in order to efficiently generate the desired optical vector fields, which makes it complicated and places high standards on SLM specifications.

In this work, we propose a simple but highly effective technique to generate a continuously varying polarization within the laser beam. This is achieved by simply having orthogonal linear polarizations on two sides of the laser beam, which is easily obtained by using a transmissive SLM with a quarter wave plate. There are many ways to record laser polarization. Recently, laser induced periodic surface structures (LIPSSs) have been shown to correlate with the incident light polarization with its groove structures either parallel or perpendicular to the laser polarization [9–14]. To demonstrate the complex polarization distribution, we focus this laser pulse onto a copper surface and produce a continuously rotating LIPSS pattern. Furthermore, we produce a number of complex surface structures where the orientation angle of the LIPSSs increases and/or decreases from left to right. The mechanism behind the evolution of the polarization distribution as the beam focuses is explained in the Jones vector formalism, and the resulting polarization distribution at the position of the ablated sample is confirmed by the simulation based on the exact transfer function approach.

Creating surface structures often has important applications in functionalization and altering material properties (e.g., optical, wetting, tribological, chemical, etc.) [15–21]. In fact, ultrafast lasers have been extensively used for surface structuring to produce micro and nano structures on material surfaces [22,23]. In our case, we use LIPSS patterns to directly record the complex rotating polarization that we produce in this work. This technique provides a very effective way to produce complex surface structures that may potentially find applications, such as polarization modulators and metasurfaces.

Figure 1 presents a schematic illustration of the experimental setup, wherein a polished copper sample is treated in ambient air using an amplified Ti:sapphire laser system. The laser system produces 65 fs pulses with a maximum pulse energy around 1 mJ/pulse at a 1 kHz repetition rate with a central wavelength of 800 nm. The power of the laser can be controlled with an attenuator consisting of a half-wave plate and a polarizer. The beam is clipped with an iris so that the clipped beam will pass through the SLM entirely. The beam vector fields are structured using the Cambridge Research & Instrumentation (CRi) SLMs with a one-dimensional array of 128 pixels.

The CRi SLM is a dual mask SLM that uses nematic liquid crystals to provide an electrically variable index of refraction for light that is polarized along the extraordinary axis of the crystal. The first mask has the extraordinary axis at 45°, and the second mask has the extraordinary axis at 135°. When two masks are driven at different voltages, the incident light will experience

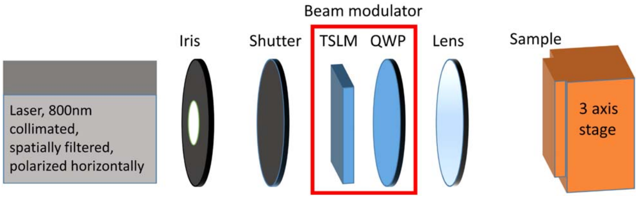

Fig. 1. Schematic diagram of the experimental setup for the spatial-variant polarization rotation and/or absolute phase modulation of the beam for surface structuring.

phase modulation based on the average of the two voltages. If a quarter wave plate with its slow axis at 0° is placed after the SLM, the difference between the voltages of the two masks will serve as the polarization rotation [1]. By keeping the absolute phase modulation constant, we induce only a spatial-variant polarization. The resulting beam vector fields are then focused with a plano-convex lens ($f = 300$ mm) at normal incidence onto the polished copper sample. All of the ablated spots in this experiment are done using 200 shots of laser pulses and an average fluence of 0.26 $\mathrm{J \cdot cm^{-2}}$ per pulse. The copper sample is mounted onto a precision three-axis manual translation system for accurate positioning in the Rayleigh range. The Rayleigh range is given by $z_R = \pi w_0^2/\lambda \approx 10$ mm, where $w_0 \approx 50$ μm is the beam waist, and $\lambda = 800$ nm is the central wavelength [24].

As the starting point, the SLM is programmed so that the left half of the beam is polarized at −90°, and the right half is polarized at 0°, as shown in Fig. 2(a). We will use the Jones vector formalism to mathematically describe the polarization distribution and its evolution as the beam propagates through various optical elements and air. The Jones matrices and vectors used in our mathematical description can be found in Ref. [25]. The Jones vector representing the polarization distribution of the beam immediately after the beam modulator is

$$\mathbf{j}_{\mathrm{out}}(x_i) = \begin{pmatrix} \Theta(i - 64.5) \\ \Theta(i - 64.5) - 1 \end{pmatrix}, \tag{1}$$

where Θ denotes the Heaviside function, and the subscript i is the pixel number of the SLM.

Because the left half and the right half of the same laser pulse are coherent, the electric field is additive. Due to diffraction, the Jones matrix of the beam after propagation through the lens is no longer described by Eq. (1). Rather, the electric fields ratio of the two orthogonal polarizations is continuously changing along the x axis. Because the left half and the right half of the beam are in phase, the normalized Jones vector at any transverse plane within the Rayleigh range must be of the form

$$\mathbf{j}_{\perp}(x, y) = \sin\theta \begin{pmatrix} 1 \\ 0 \end{pmatrix} + \cos\theta \begin{pmatrix} 0 \\ -1 \end{pmatrix}, \tag{2}$$

where $0 \le \theta \le 90°$ and $\tan\theta = E_{0°}/E_{-90°} \ge 0$ are the local electric fields ratio of the 0° linearly polarized beam to the −90° linearly polarized beam. This ratio is a monotonically increasing function of x before the focus, so the spatially varying polarization must be linearly polarized at angles monotonically increasing from −90° to 0° as a function of x. Figure 2(d) presents the scanning electron microscope (SEM) image of the induced pattern irradiated at 3.5 mm before the focal plane

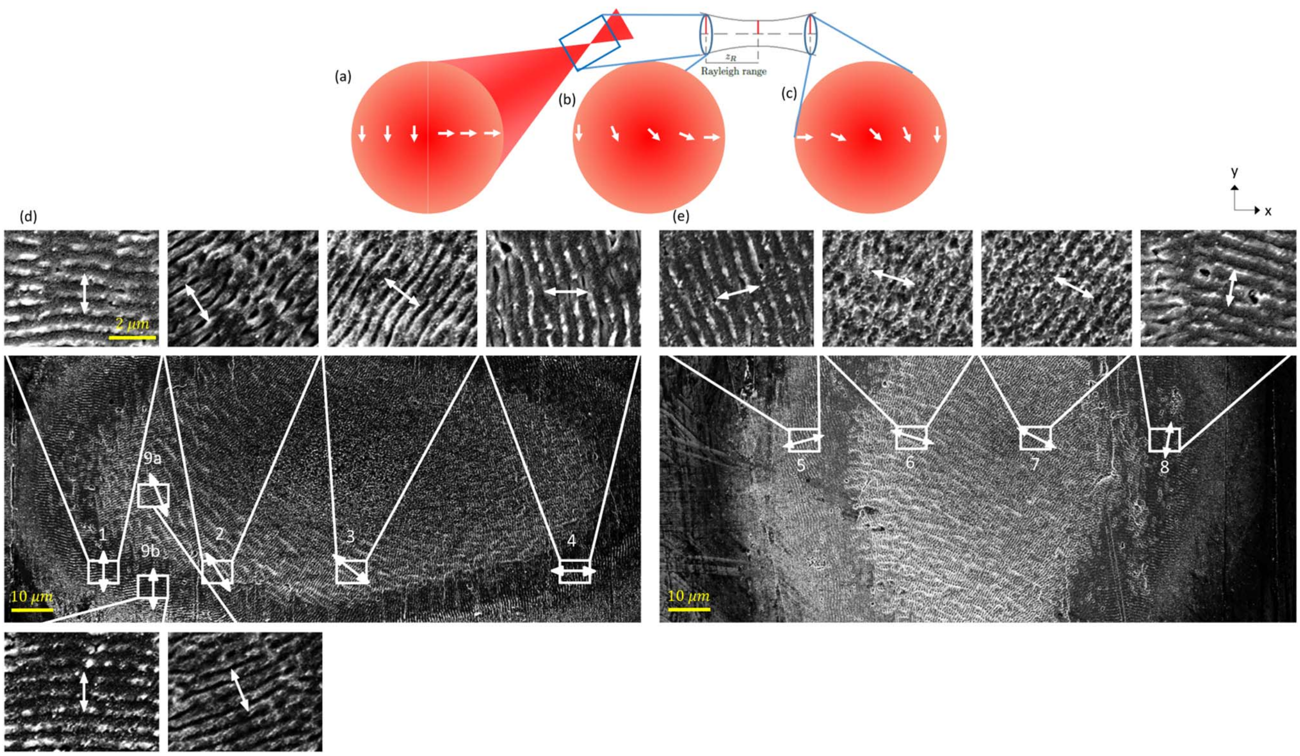

Fig. 2. Polarization distribution (a) immediately after the beam modulator, (b) before, and (c) after the focal plane at the Rayleigh range. (d) SEM image of the induced pattern irradiated at 3.5 mm before the focal plane by focusing a collimated beam with two sections of polarization, as shown in (a). (e) SEM image of the induced pattern irradiated at 0.5 mm after the focal plane under the same experimental conditions. The scale bars are the same for all of the zoomed-in images.

by focusing a collimated beam with two sections of polarization, as shown in Fig. 2(a). The LIPSSs with periodicity $\Lambda \sim \lambda$ are oriented orthogonal to the local electric field vectors, providing a direct method of analyzing polarization [11–13]. Curved LIPSSs are formed due to diffraction instead of having two sections of ripples that are oriented orthogonally.

It is evident that the LIPSSs angle changes from left to right. In addition, this technique can also create curved LIPSSs along the y direction. As shown in the magnified images of region 9a and region 9b in Fig. 2(d), the polarization angle is different despite having the same x position. This is because the beam shape is elliptical. The left edge of the beam is a 180° arc. The region 9b lies at the left edge of the beam, which is linear polarized at −90°, while region 9a is located to the right of the left edge. Hence, the polarization angle in this region is −70°.

In order to further affirm the validity of our idea, we perform the experiment again with the sample placed after the focal plane. By simple ray tracing, the beam will be inverted after the focus. In other words, the polarization distribution and the pattern irradiated become inverted. Figure 2(c) presents this inverted polarization distribution, and Fig. 2(e) presents the SEM image of the induced pattern irradiated 0.5 mm after the focal plane. Indeed, the induced pattern verifies the inversion of the polarization distribution.

The versatility of the proposed idea is demonstrated by creating a few more complex surface structures using different polarization distributions. Figures 3(d)–3(g) show regions 1 to 4 of the SEM images of the induced pattern irradiated at 3.5 mm before the focal plane by focusing a collimated beam with two sections of polarization, as shown in Fig. 3(a). The left half of the beam is polarized at 90°, and the right half is polarized at 0° immediately after the beam modulator. Going through the same analysis as mentioned above, the spatially varying polarization must be linearly polarized at angles monotonically decreasing from 90° to 0°, resembling the polarization distribution of Fig. 3(b). Figures 3(h)–3(k) show regions 5 to 8 of the SEM image of the induced pattern irradiated 0.5 mm after the focal plane. The spatially varying polarization is linearly polarized at angles monotonically increasing from 0° to 90° as a function of x, resembling the polarization distribution of Fig. 3(c). Again, the irradiated pattern confirms the inversion of the polarization distribution. As shown in Figs. 2 and 3, we can fabricate curved LIPSSs with angles monotonically increasing or decreasing both before and after the focus.

Next, we further demonstrate our idea by splitting the polarization distribution of the laser beam into three sections. Figures 4(d)–4(g) display regions 1 to 4 of the SEM images of the induced pattern irradiated at 3.5 mm before the focal plane by focusing a collimated beam with three sections of polarization, as shown in Fig. 4(a). The left portion of the beam is polarized at −90°, the middle portion is polarized at 0°, and the right portion of the beam is polarized at −90° immediately after the beam modulator. Based on similar analyses, the spatially varying polarization must be linearly polarized at angles monotonically increasing from −90° to some finite angle k and then monotonically decreasing from k to −90°, resembling Fig. 4(b). This is because the electric fields ratio $E_{-90°}/E_{0°}$ is non-zero at the center. As shown in Fig. 4(e), $k \approx -50°$ and agrees with the explanation. Figures 4(h)–4(k) reveal regions 5 to 8 of the SEM image of the induced pattern irradiated 0.5 mm after the focal plane. The polarization distribution should be inverted. However, the polarization distribution remains the same after the inversion due to symmetry. Despite this symmetry, the LIPSSs angle shows that the polarizations are linearly polarized at angle −50° in regions 5 to 8. This is because the ablated spot is very close to the focus, where the two orthogonal polarizations have the most significant overlap.

In order to confirm the evolution of the polarization distribution, we simulate the propagation of electromagnetic waves using the exact transfer function approach. The electric field

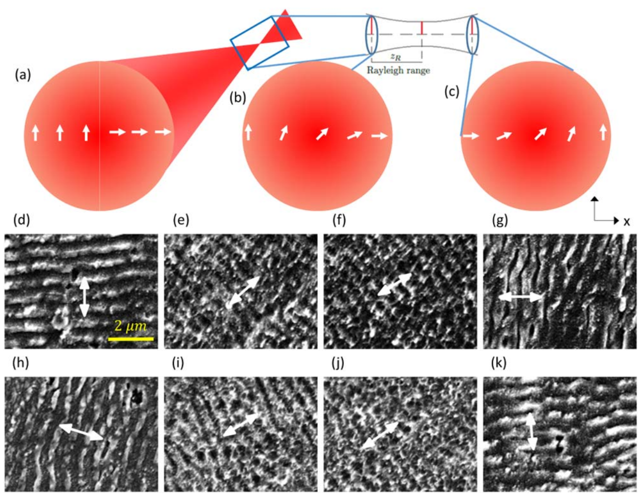

Fig. 3. Polarization distribution (a) immediately after the beam modulator, (b) before, and (c) after the focal plane at the Rayleigh range. (d)–(g) Regions 1 to 4 of the SEM images of the induced pattern irradiated at 3.5 mm before the focal plane by focusing a collimated beam with two sections of polarization, as shown in (a). (g)–(k) Regions 5 to 8 of the SEM images of the induced pattern irradiated at 0.5 mm after the focal plane under the same experimental conditions. The scale bars are the same for all of the SEM images.

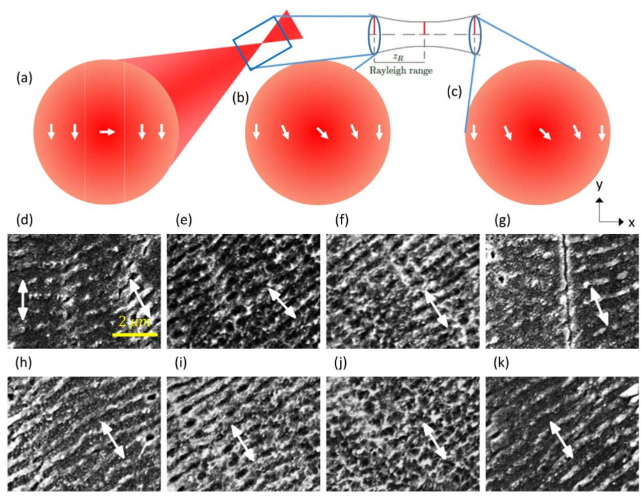

Fig. 4. Three sections design. Polarization distribution (a) immediately after the beam modulator, (b) before, and (c) after the focal plane at the Rayleigh range. (d)–(g) Regions 1 to 4 of the SEM images of the induced pattern irradiated at 3.5 mm before the focal plane by focusing a collimated beam with three sections of polarization, as shown in (a). (g)–(k) Regions 5 to 8 of the SEM images of the induced pattern irradiated at 0.5 mm after the focal plane under the same experimental conditions. The scale bars are the same for all of the SEM images.

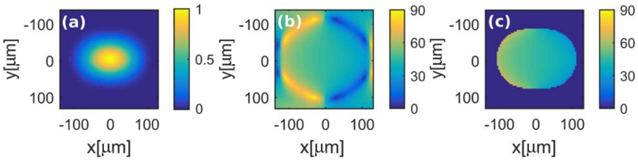

Fig. 5. (a) Simulated normalized intensity distribution and (b) polarization distribution at 3.5 mm before the focal plane. The initial polarization distribution is Fig. 2(a). (c) Clipped version of polarization distribution at the ablation area.

distribution at distance z ($U(x, y, z)$) propagated from the electric field at the initial plane $z = 0$ ($U(x, y, 0)$) is calculated as follows:

$$U(x, y, z) = \mathcal{F}^{-1}\{\mathcal{F}\{U(x, y, 0)\} \times \exp\{i2\pi z\lambda^{-1}[1 - (\lambda f_X)^2 - (\lambda f_Y)^2]^{1/2}\}\}, \quad \textbf{(3)}$$

where $\mathcal{F}\{\}$ indicates the Fourier transform, λ is the wavelength of the electromagnetic wave, and f_X, f_Y are the sampling rate in the frequency domain [26].

Using a self-made Matlab code, the electric field can be simulated using Eq. (3) and discrete Fourier transform. The electric field at the initial plane is defined as

$$U(x, y, 0) = \exp\left(-\frac{x^2}{2\sigma_x^2} - \frac{y^2}{2\sigma_y^2} + i\pi\frac{x^2 + y^2}{\lambda f}\right)\mathrm{circ}\left(\frac{\sqrt{x^2 + y^2}}{\rho}\right), \quad \textbf{(4)}$$

where $\sigma_x = 4$ mm and $\sigma_y = 1$ mm are the standard deviation of the Gaussian beam, $f = 30$ cm is the focal length of the lens, and $\rho = 2$ mm is the semi-aperture of the beam.

The beam is then split into two half-disks, such that the left half is vertically polarized, and the right half is horizontally polarized, as shown in Fig. 2(a):

$$U_V(x, y, 0) = -U(x, y, 0)\Theta(-x), \quad \textbf{(5)}$$

$$U_H(x, y, 0) = U(x, y, 0)\Theta(x). \quad \textbf{(6)}$$

In the simulation, they are both propagated to a user-chosen distance z, and electric field is added as a vector sum. The intensity distribution $I(x, y, z)$ and the polarization angle $\phi(x, y, z)$ can be calculated by

$$I(x, y, z) = U_V(x, y, z)^2 + U_H(x, y, z)^2, \quad \textbf{(7)}$$

$$\phi(x, y, z) = -\arctan\left(\frac{|U_V(x, y, z)|}{|U_H(x, y, z)|}\right). \quad \textbf{(8)}$$

Figure 5 shows the simulation result, which agrees well with the experimental result; the polarization continuously and gradually changes over the range from left to right, and the beam shape is elongated horizontally due to diffraction.

To conclude, this study demonstrates a novel and simple method for generating a continuously varying polarization by combining two or three sections of orthogonal polarizations within a laser beam. To demonstrate this complex polarization distribution, we apply the laser beam onto a metal surface to create a continuously rotating LIPSS pattern. This technique provides a very effective way to produce complex surface structures that may potentially find applications, such as polarization modulators and metasurfaces.

Funding. Army Research Office (ARO) (W911NF-15-1-0319); Bill and Melinda Gates Foundation (OPP1119542); Boeing; AlchLight.

REFERENCES

1. W. Han, Y. Yang, W. Cheng, and Q. Zhan, Opt. Express **21**, 20692 (2013).
2. J. Ouyang, W. Perrie, O. J. Allegre, T. Heil, Y. Jin, E. Fearon, D. Eckford, S. P. Edwardson, and G. Dearden, Opt. Express **23**, 12562 (2015).
3. K. Lou, S. X. Qian, X. L. Wang, Y. Li, B. Gu, C. Tu, and H. T. Wang, Opt. Express **20**, 120 (2012).
4. K. K. Anoop, A. Rubano, R. Fittipaldi, X. Wang, D. Paparo, A. Vecchione, L. Marrucci, R. Bruzzese, and S. Amoruso, Appl. Phys. Lett. **104**, 241604 (2014).
5. O. J. Allegre, W. Perrie, S. P. Edwardson, G. Dearden, and K. G. Watkins, J. Opt. **14**, 085601 (2012).
6. G. D. Tsibidis, E. Skoulas, and E. Stratakis, Opt. Lett. **40**, 5172 (2015).
7. C. Hnatovsky, V. Shvedov, and W. Krolikowski, Opt. Express **21**, 12651 (2013).
8. O. J. Allegre, Y. Jin, W. Perrie, J. Ouyang, E. Fearon, S. P. Edwardson, and G. Dearden, Opt. Express **21**, 21198 (2013).
9. J. Bonse, J. Krüger, S. Höhm, S. V. Kirner, and A. Rosenfeld, J. Laser Appl. **24**, 042006 (2012).
10. J. Bonse, S. Höhm, S. V. Kirner, A. Rosenfeld, and J. Kruger, IEEE J. Sel. Top. Quantum Electron. **23**, 1 (2016).
11. J. Bonse, A. Rosenfeld, and J. Krüger, J. Appl. Phys. **106**, 104910 (2009).
12. J. Wang and C. Guo, Appl. Phys. Lett. **87**, 251914 (2005).
13. A. Y. Vorobyev, V. S. Makin, and C. Guo, J. Appl. Phys. **101**, 034903 (2007).
14. Y. Shimotsuma, P. G. Kazansky, J. Qiu, and K. Hirao, Phys. Rev. Lett. **91**, 247405 (2003).
15. A. Y. Vorobyev and C. Guo, Adv. Mech. Eng. **2**, 452749 (2010).
16. A. Y. Vorobyev and C. Guo, Laser Photon. Rev. **7**, 385 (2013).
17. T. Baldacchini, J. E. Carey, M. Zhou, and E. Mazur, Langmuir **22**, 4917 (2006).
18. A. Y. Vorobyev and C. Guo, Phys. Rev. B **72**, 195422 (2005).
19. A. Y. Vorobyev and C. Guo, Appl. Phys. Lett. **92**, 041914 (2008).
20. A. Mizuno, T. Honda, J. Kiuchi, Y. Iwai, N. Yasumaru, and K. Miyazaki, Tribol. Online **1**, 44 (2006).
21. N. Yasumaru, K. Miyazaki, and J. Kiuchi, Appl. Surf. Sci. **254**, 2364 (2008).
22. R. Le Harzic, D. Breitling, M. Weikert, S. Sommer, C. Föhl, S. Valette, C. Donnet, E. Audouard, and F. Dausinger, Appl. Surf. Sci. **249**, 322 (2005).
23. D. Breitling, A. Ruf, and F. Dausinger, Proc. SPIE **5339**, 49 (2004).
24. H. N. Damask, *Polarization Optics in Telecommunications*, 1st ed. (Springer, 2004).
25. D. H. Goldstein, *Polarized Light*, 3rd ed. (CRC Press, 2011).
26. J. W. Goodman, *Introduction to Fourier Optics*, 3rd ed. (Ben Roberts, 2005).